GEOPHYSICS

# Global variations of large megathrust earthquake rupture characteristics

Lingling Ye,[1,2]* Hiroo Kanamori,[2] Thorne Lay[3]



**Despite the surge of great earthquakes along subduction zones over the last decade and advances in observations and analysis techniques, it remains unclear whether earthquake complexity is primarily controlled by persistent fault properties or by dynamics of the failure process. We introduce the radiated energy enhancement factor (REEF), given by the ratio of an event's directly measured radiated energy to the calculated minimum radiated energy for a source with the same seismic moment and duration, to quantify the rupture complexity. The REEF measurements for 119 large [moment magnitude ($M_w$) 7.0 to 9.2] megathrust earthquakes distributed globally show marked systematic regional patterns, suggesting that the rupture complexity is strongly influenced by persistent geological factors. We characterize this as the existence of smooth and rough rupture patches with varying interpatch separation, along with failure dynamics producing triggering interactions that augment the regional influences on large events. We present an improved asperity scenario incorporating both effects and categorize global subduction zones and great earthquakes based on their REEF values and slip patterns. Giant earthquakes rupturing over several hundred kilometers can occur in regions with low-REEF patches and small interpatch spacing, such as for the 1960 Chile, 1964 Alaska, and 2011 Tohoku earthquakes, or in regions with high-REEF patches and large interpatch spacing as in the case for the 2004 Sumatra and 1906 Ecuador-Colombia earthquakes. Thus, combining seismic magnitude $M_w$ and REEF, we provide a quantitative framework to better represent the span of rupture characteristics of great earthquakes and to understand global seismicity.**

## INTRODUCTION

Rupture characteristics of large earthquakes on subduction zone plate boundary faults vary substantially (*1*–*3*). Earth's largest earthquakes, such as the 1960 Chile [moment magnitude ($M_w$) 9.5], 1964 Alaska ($M_w$ 9.2), 2004 Sumatra ($M_w$ 9.2), and 2011 Tohoku, Japan ($M_w$ 9.1) events, have all involved large rupture areas but have very different total rupture durations and slip distributions. The 2004 Sumatra earthquake ruptured multiple isolated asperities (regions of large coseismic slip) along strike for about more than 8 min, whereas the similar-magnitude 2011 Tohoku earthquake had a single dominant large-slip patch near the trench that produced a huge tsunami and ruptured for about 3 min. Other large events show regional variations in rupture complexity even if large-slip areas are similar in dimensions, indicating the need for a more nuanced characterization of large earthquake ruptures including an evaluation of whether rupture properties of asperities differ from region to region. Small earthquakes are also found to have substantial slip complexity (*4*); rupture complexity exists across all scales.

What controls large earthquake complexity remains an open question (*5*). Many studies have explored the influence of subduction zone parameters on great megathrust earthquakes (*1*, *6*, *7*), but these do not directly consider rupture complexity. Repeating earthquakes (*8*, *9*), geodetic measurements of interseismic strain accumulation (*10*), and numerical fault modeling (*11*) support the notion of some frictionally locked asperities being surrounded by creeping regions with different frictional properties (*12*). There is evidence for persistent behavior of ruptures through multiple earthquake cycles: (i) geological evidence of similar large slip in giant earthquakes preceding the 1960 Chile and 1964 Alaska events with relatively regular intervals of several hundred to several thousand years (*13*, *14*); (ii) quasi-repeating large earthquakes with intervals of several decades, such as the 1942 and 2016 $M_w$ ~7.8 Ecuador earthquakes (*15*) and the 1952 and 2003 Tokachi-oki $M_w$ ~8.3 earthquakes (*16*); and (iii) semiregularly repeating small earthquakes, such as on the San Andreas fault at Parkfield (*8*) and in the Kamaishi region, offshore of Honshu (*9*). Persistent behavior of asperities and adjacent zones of aseismic slip may determine characteristic slip patch attributes of each subduction boundary. However, it has also been recognized that great earthquakes exhibit noncharacteristic behavior involving variable rupture of multiple slip patches (*15*), as has been demonstrated by the Ecuador-Colombia earthquakes in 1906, 1942-1958-1979-1998, and 2016 and the great earthquake sequence along the Nankai trough, Japan (*17*). Strong acceleration of small to moderate repeating earthquakes due to changing boundary conditions, such as deformation rates after great earthquakes, has also been widely observed (*18*, *19*). Numerical models suggest that increased complexity can exist in systems with a relatively simple distribution of friction properties due to interaction of nearby slip patches (*20*). It is unclear whether earthquake complexity is determined by geological factors or results entirely from the dynamics of earthquake ruptures. In the former case, earthquake complexity should show more systematic spatial variations.

## METHODS

We seek a seismological parameter to improve characterization of rupture complexity. Radiated energy ($E_R$) is closely related with rupture complexity, and the measurement accuracy of $E_R$ has greatly improved with the recent availability of large global broadband data sets (figs. S4 and S5) (*21*). We need a reference measure to make it scale-independent. The most widely used measure is seismic moment ($M_0$)–scaled radiated energy, $E_R/M_0$, which is a clear indicator of anomalous tsunami earthquakes but does not exhibit clear regional variation (Fig. 1) or

[1]School of Earth Sciences and Engineering, Sun Yat-sen University, Guangzhou 510275, China. [2]Seismological Laboratory, California Institute of Technology, Pasadena, CA 91125, USA. [3]Department of Earth and Planetary Sciences, University of California, Santa Cruz, Santa Cruz, CA 95064, USA.
*Corresponding author. Email: lingling@gps.caltech.edu

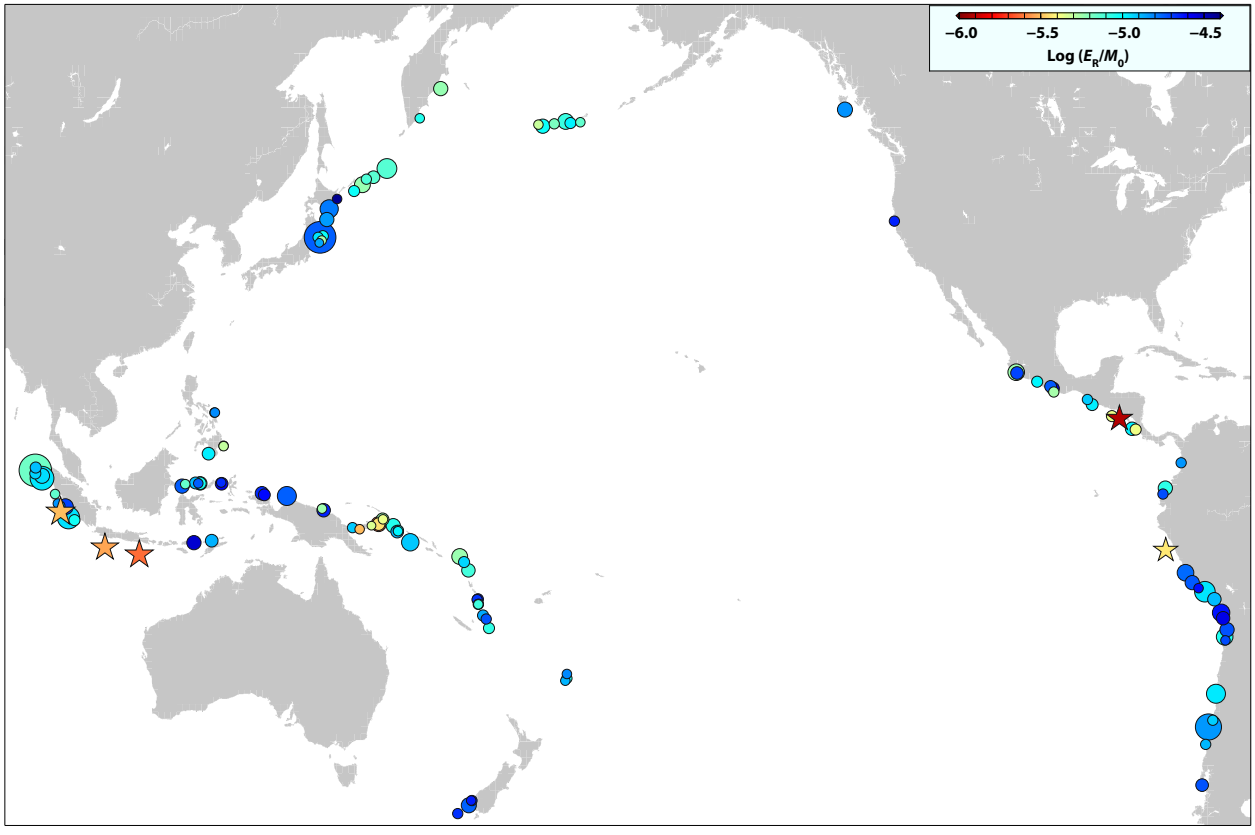


**Fig. 1. Map of seismic moment–scaled radiated energy variation for 119 global large megathrust earthquakes from 1990 to 2016.** The radiated energy is based on the broadband source spectrum of the frequency band from 0.005 to 1 Hz. Stars indicate large tsunami earthquakes. The size of circles and stars is scaled with the earthquake magnitude.

earthquake magnitude dependence (*21*), despite having approximately two orders of magnitude variation. This parameter does not capture the difference in documented rupture complexity between the 2004 Sumatra and 2011 Tohoku earthquakes noted above. Other source parameters, such as static stress drop, are highly dependent on the measurement procedure and have large scatter, without systematic regional patterns (fig. S1) (*21*), making them difficult to use to characterize rupture complexity.

We introduce another scale-independent energy parameter, radiated energy enhancement factor (REEF), to characterize rupture complexity. REEF is defined by $E_R/E_{R\_min}$, where $E_{R\_min}$ is a theoretical minimum value of radiated energy ($E_R$) for a given seismic moment ($M_0$) and duration ($T$), and is given by

$$E_{R\_min} = \frac{6}{5\rho\pi\beta^5}\frac{M_0^2}{T^3} \quad (1)$$

where ρ and β are density and shear wave velocity around the source, respectively (*22*). The moment-rate function (MRF) that gives $E_{R\_min}$ has a parabolic shape (Fig. 2C) given by

$$\dot{M}(t) = 6M_0/T^3 \cdot t \cdot (T - t) \quad (2)$$

Actual earthquakes always have higher $E_R$ because their MRFs are more complex than the parabolic shape for the $E_{R\_min}$ reference case. REEF simply measures the radiated energy in units of the minimum energy for the given seismic moment and duration and can be computed across a wide range of earthquake sizes once radiated energy, seismic moment, and source duration are estimated.

Because REEF can be written as

$$\text{REEF} \equiv \frac{E_R}{E_{R\_min}} = \frac{E_R}{M_0} \cdot \frac{M_0}{E_{R\_min}} \propto \frac{E_R}{M_0} \cdot \frac{T^3}{M_0} \quad (3)$$

it can be expressed as a product of the seismic moment–scaled radiated energy and the moment-scaled cube of the duration, both of which have been extensively investigated in seismology. $E_R/M_0$ is related to the apparent stress, which is the product of the average stress and seismic efficiency (*21*), and is not necessarily related directly to rupture complexity. As shown in Fig. 3A, it is only weakly correlated to REEF. In contrast, for simple dislocation models, $T^3/M_0$ is determined by rupture geometry and $V_r^3\Delta\sigma$ ($V_r$, rupture speed; $\Delta\sigma$, static stress drop) (*21*). Relatively strong correlation between REEF and $T^3/M_0$ (Fig. 3B and fig. S2) suggests that seismic energy radiation was largely controlled by spatial and temporal irregularities. Equation 3 indicates that REEF is a parameter combining the three source parameters, seismic moment $M_0$, radiated energy $E_R$, and source duration $T$, to represent the rupture complexity through energy radiation. Combining uncertainties in estimating rupture duration and radiated energy, the uncertainty of the relative REEF values across the population in this study is about a factor of 2 (see details in the Supplementary Materials).

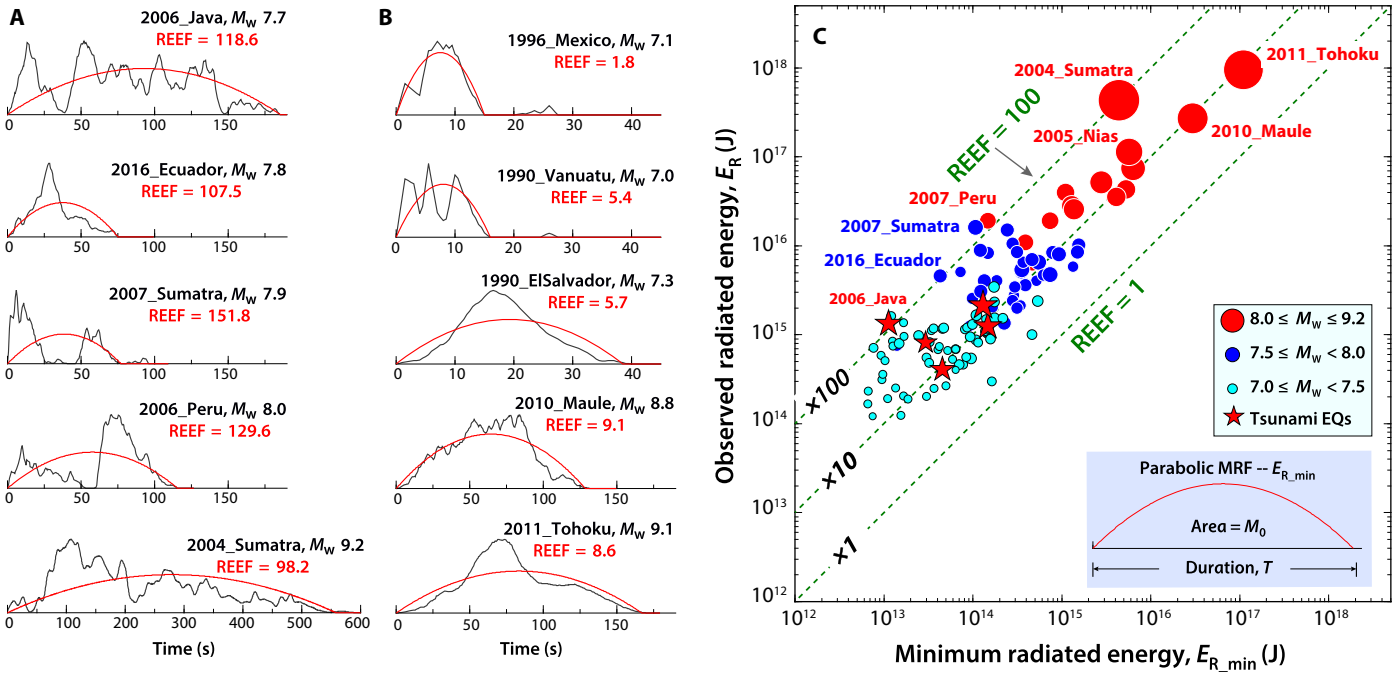


**Fig. 2. Examples of MRFs and REEF.** (**A** and **B**) Examples of MRFs for earthquakes with high and low REEF values, respectively. (**C**) Observed radiated energy $E_R$ versus calculated minimum radiated energy $E_{R\_min}$ for 119 global large megathrust earthquakes from 1990 to 2016. Red stars indicate tsunami earthquakes. The size of circles and stars is scaled with the earthquake seismic magnitude. Red, blue, and cyan circles are for three magnitude bins, $M_w$ 8.0 to 9.2, 7.5 to 8.0, and 7.0 to 7.5, respectively. Three dashed lines show REEF values of 1, 10, and 100, respectively. The bottom right insert shows the parabolic shape of an MRF for minimum radiated energy for a given seismic moment and source duration. REEF varies from ~5 to 150 for all magnitude ranges considered.

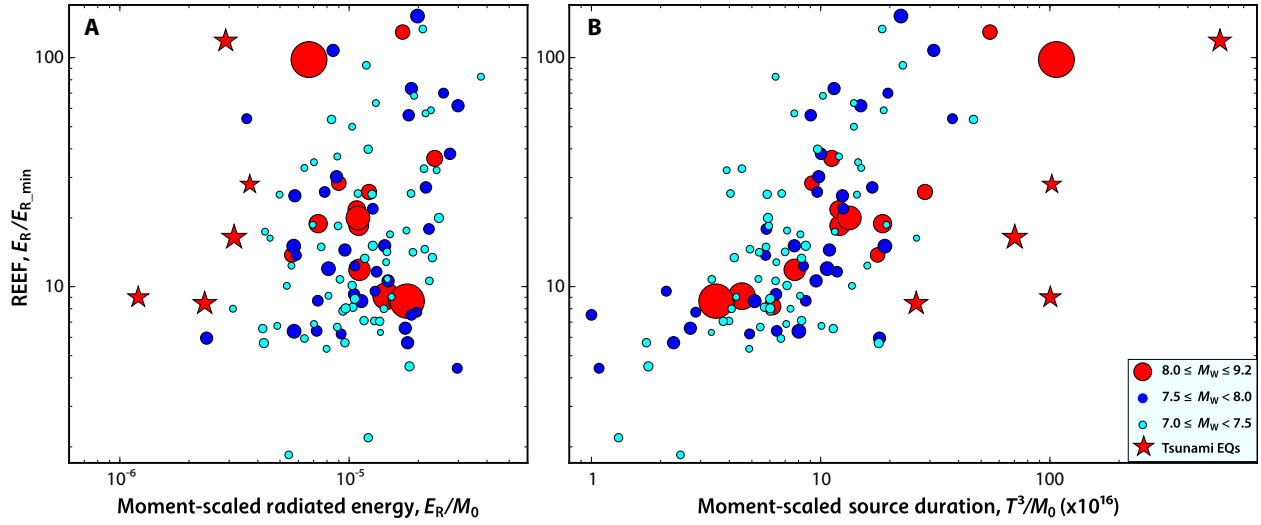


**Fig. 3. Comparison of REEF and other measures.** Variation of REEF with (**A**) seismic moment–scaled radiated energy and (**B**) moment-scaled cubed source duration. Red stars indicate tsunami earthquakes (EQs). The size of circles and stars is scaled with the earthquake magnitude. Red, blue, and cyan circles are for three magnitude bins, $M_w$ 8.0 to 9.2, 7.5 to 8.0, and 7.0 to 7.5, respectively. Variation of REEF values correlates with moment-scaled cubed duration, with little overall dependence on moment-scaled radiated energy, but REEF explicitly combines the radiated energy and source duration information to give a distinct measure of radiated energy variation between events.

Because of the relationship between radiated energy and the source MRF, $E_R \propto \int_0^T \ddot{M}(t)^2 dt$, REEF is related to measures of the roughness of the MRF (details in the Supplementary Materials; figs. S7 to S9). Earthquakes with rough MRFs tend to have a high REEF value (Fig. 2A), whereas those with simple and smooth MRFs tend to have a low REEF value (Fig. 2B). Because MRFs obtained by finite-fault inversion cannot be determined accurately at the high frequencies that convey much of the radiated energy (fig. S8), discrepancies between REEF and MRF roughness exist, such as for the 2016 Ecuador earthquake (Fig. 2A).

Thus, the MRF comparisons in Fig. 2 are intended only for illustration purposes. Although we used MRF estimates to evaluate the low-frequency contribution to radiated energy, the primary measurement is directly from broadband ground velocities, which are not as severely band-limited (*21*).

## RESULTS

For 119 large megathrust earthquakes with systematically measured radiated energy (*21*), we find that REEF varies from about 5 to 150 (Fig. 2C). The complex 2004 Sumatra rupture has much higher REEF value of 98 compared to the smooth ruptures of the 2011 Tohoku (REEF = 8.6) and 2010 Maule (REEF = 9.1) earthquakes. REEF variation is also substantial among shallow tsunami earthquakes. Rupture of multiple asperities is responsible for the very high REEF value of 119 for the 2006 Java tsunami earthquake (*23*). The large range of REEF indicates that it is a sensitive measure of rupture complexity. Variation exists in each of three magnitude bins: $M_w$ ~7.0 to7.5, 7.5 to 8.0, and 8.0 to 9.2, suggesting that rupture complexity is independent of earthquake magnitude. Given our limited magnitude range from 7 to 9.2, we cannot resolve how far this self-similarity may extend.

REEF for $M_w$ 7 to 8 earthquakes represents the slip characteristics of patches with length scales of 50 to 150 km. The precise dynamic rupture properties controlling the REEF value for each event remain unresolved, but REEF values exhibit systematic regional variations (Fig. 4), most strikingly along the eastern Pacific subduction zones. From southern Mexico to Middle America, where uniformly weak interseismic coupling has been inferred (*24*), earthquakes consistently have low values. The 1992 $M_w$ 7.6 Nicaragua tsunami earthquake with multiple asperities (*24*) has a slightly higher value (~9) compared to the average regional REEF (~5.5). From Colombia to northern Chile, earthquakes have uniformly high REEF values, in a region with strong spatial heterogeneity of interseismic coupling (*15*, *25*, *26*). Events with very high REEF compared to the average (~38), such as 2007 Peru (REEF = 130) (*3*) and 2016 Ecuador (REEF = 108) (*15*) earthquakes, have compound ruptures with multiple well-separated asperities. In southern Chile, three events, including the 2010 Maule earthquake, have low values in a region with relatively uniform strong coupling (*10*).

REEF values for earthquakes along the Japan and Kuril trenches are less uniform, varying from lower values in the south to higher values in the north. A change in values occurs near the disruption of the island arc structure (Bussol graben) between the great 1963 $M_w$ 8.5 event and the

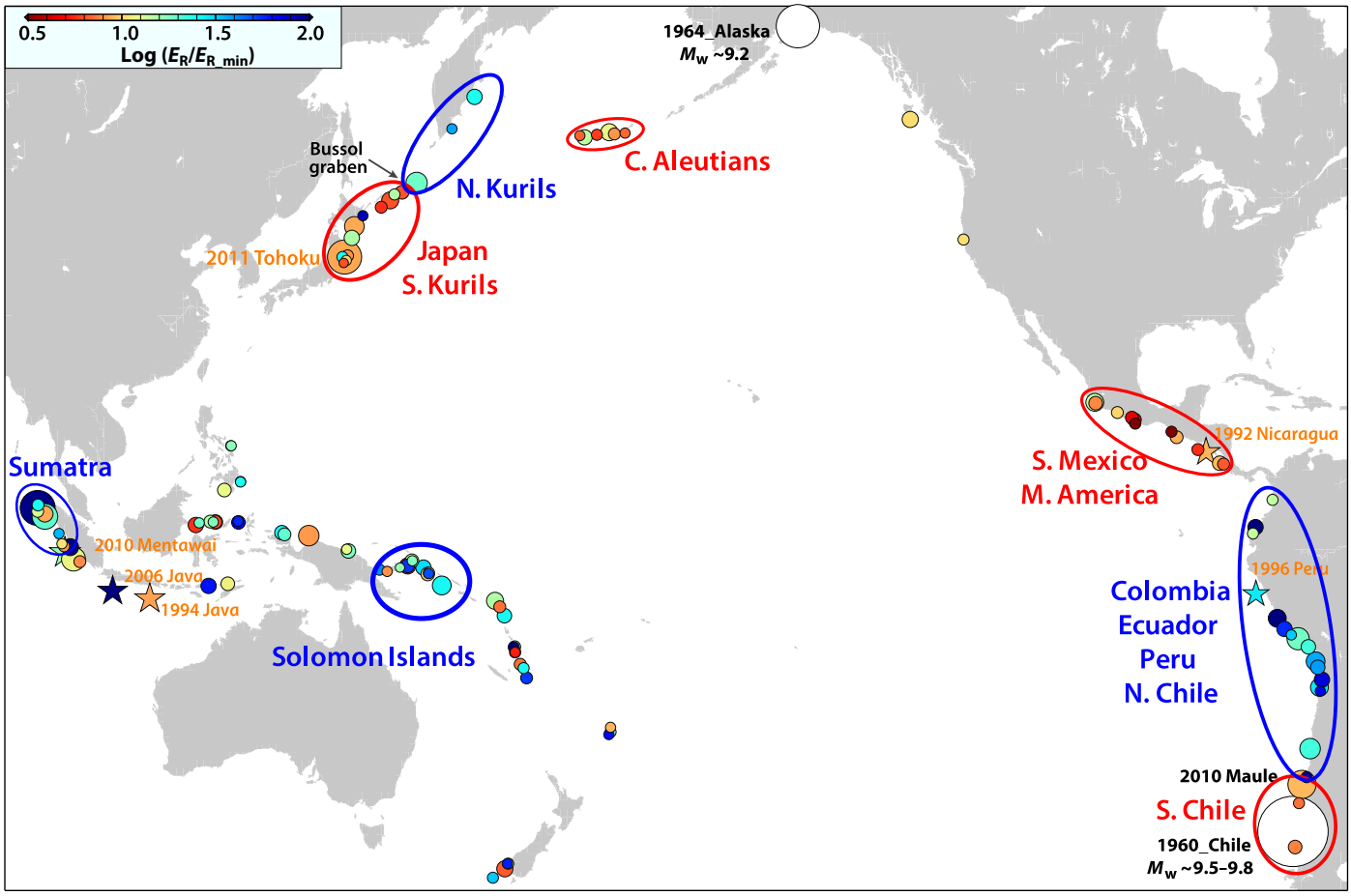


**Fig. 4. Map view of REEF values for 119 global large megathrust earthquakes.** Earthquakes are color-coded by the corresponding REEF values in $\log_{10}$ scale. Note systematic REEF for some regions, such as high values for Colombia–Ecuador–Peru–northern Chile (N. Chile), northern Kurils (N. Kurils), Solomon Islands, and Sumatra and low values at southern Mexico (S. Mexico)–Middle America (M. America), southern Chile (S. Chile), northern Japan (N. Japan)–southern Kurils (S. Kurils), and central Aleutians (C. Aleutians). Stars are for large tsunami earthquakes. Two white circles show the 1960 Chile and 1964 Alaska earthquakes. Symbol sizes are scaled with earthquake magnitude.

2006–2007 ($M_w$ 8.4 to 8.1) sequence (*27*). Several events in the central Aleutians overlap portions of the 1957 $M_w$ 8.9 and 1965 $M_w$ 8.7 earthquakes and have relatively low REEF values. Slightly higher REEF values for two $M_w$ ~7.8 events (~12 to 15), than for four $M_w$ ~7.0 events (~5 to 8), are associated with compound ruptures indicated by slip models (*21*, *28*). For subduction zones in the Southwest Pacific and along Sumatra, values fluctuate, which is likely due to the great variation in structure along the trench; overall a high REEF value might be associated with a high degree of megathrust segmentation along strike. In the Solomon Islands, high REEF values may result from high susceptibility to triggering in this region with events having moderate-size slip patches discretely distributed with spacing that promotes temporal clustering, if not coincident failure (*3*). Earthquakes in Sumatra tend to have large REEF, especially to the north near the 2004 Sumatra earthquake. REEF values are enhanced for the 2004 $M_w$ 9.2 (98) and 2007 $M_w$ 7.9 (152) Sumatra earthquakes, which have well-separated asperities, compared to the average for the entire Sumatra area (REEF ~20).

Although REEF measures have significant scatter, Fig. 4 shows four subduction zones with systematically low REEF values averaging around 5 to 10 and four regions with systematically high values averaging around 20 to 50 (fig. S6). The systematical regional variation suggests that, in addition to different asperity sizes and spacing as described in the conventional asperity model, the rupture character of asperities might be regionally different.

## DISCUSSION

To provide a conceptual framework categorizing the wide range of REEF measurements for different subduction zones (Fig. 4), we propose a modified asperity representation (Fig. 5) involving regional variation of asperity maximum size, spacing, and rupture character based on REEF observations. The left-most column follows the same scheme as the conventional asperity model (*1*). From top to bottom, interasperity spacing increases and maximum asperity size decreases (see the Supplementary Materials). To characterize each region, we introduce a parameter, $R_C$, which is the ratio of asperity area to the total area of the region considered (the rectangular box in Fig. 5). Large $R_C$ values indicate more uniform coupling with small spacing between asperities, whereas small $R_C$ values indicate more heterogeneous coupling with large spacing. For simplicity and illustration purposes, we assume that the asperities in each region have the same size and $R_C$ decreases proportional to $1/n$. Then, the size of a single asperity decreases as $1/n^2$, and the spacing between asperities increases correspondingly, proportional to $(n-1)/n^2$ for a one-dimensional asperity distribution and $\sqrt{(n-1)/n^2}$ for a two-dimensional asperity distribution. The corresponding variations of the characteristic earthquake size are shown in table S1.

The left and right halves of our modified asperity model involve asperity ruptures with low and high REEF values, respectively. Triggering of multiple asperities increases REEF for both categories. The main difference between low and high REEF cases is that triggering is more

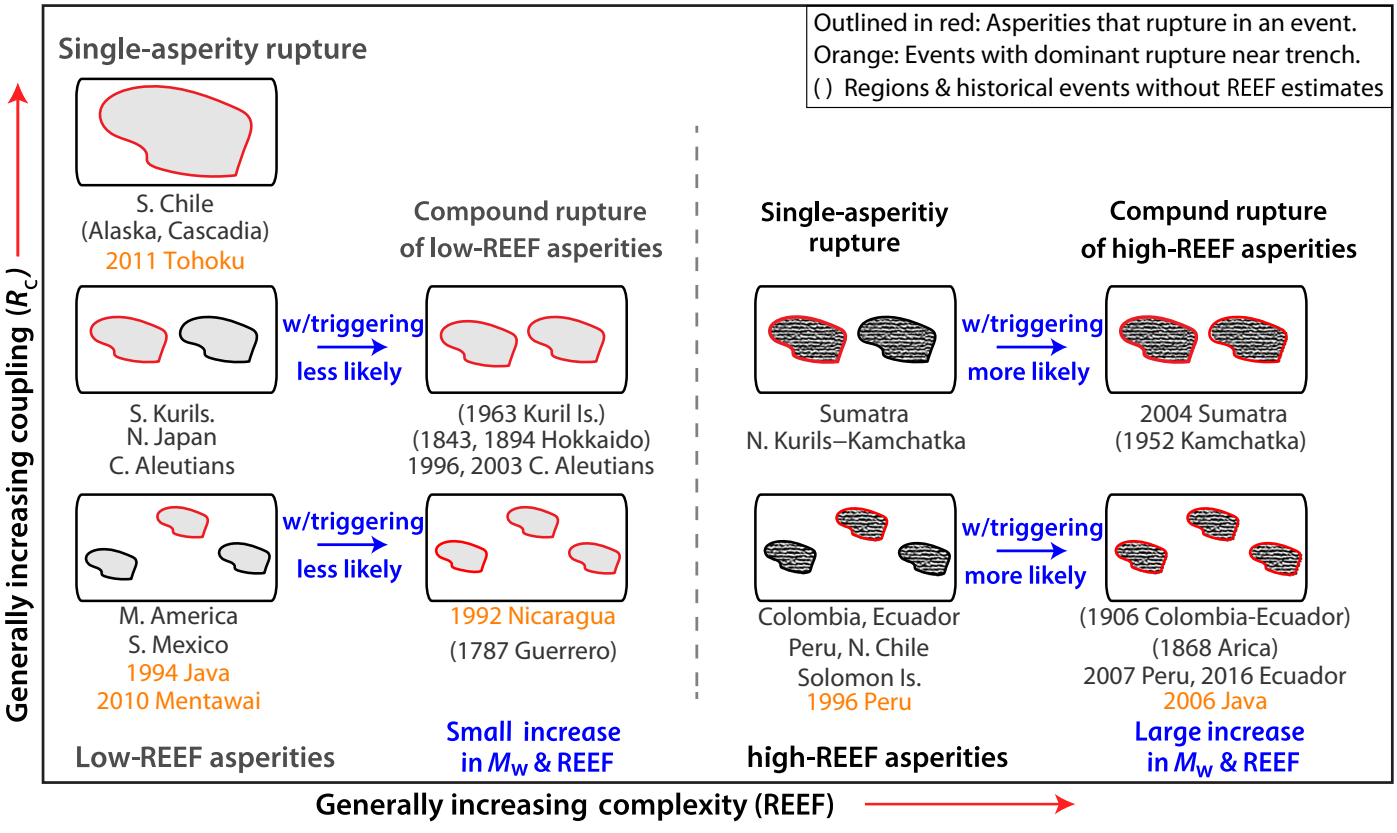


**Fig. 5. Schematic categorization of ruptures associated with varying REEF and $R_C$ values.** Regions with slip patches of varying size and spacing, indicating variable fraction of asperity area $R_C$, can have ruptures that either produce low REEF values (left side, with light shading indicating smooth, simple rupture) or produce high REEF values (right side, with dark shading indicating rough, complex ruptures). Individual slip patches may fail or they may trigger additional slip patches, which increases REEF and earthquake magnitude overall within either category. Rough regions are more likely to have compound rupture due to triggering with relatively larger increases in magnitude and REEF. Below each schematic, specific subduction zones and events in that category are listed. Earthquakes labeled in orange are dominated by the near-trench rupture. Labeled regions or earthquakes in parentheses lack REEF measurements but are assigned to categories based on qualitative rupture attributes. Kuril Is., Kuril Islands; Solomon Is., Solomon Islands.

likely to occur in high-REEF regions because failure of high-REEF asperities involves higher energy release. We now consider details of this framework.

Individual slip patches may have low REEF (left side in Fig. 5) or high REEF values (right side in Fig. 5). We consider four basic combinations, recognizing that there can be a continuum of intermediate cases:

Case 1. Low REEF value (smooth asperity/rupture) and high $R_C$ (small separation, uniform)

In this case, relatively smooth and uniform great earthquake ruptures are likely to occur in moderate to high plate coupling environments. Southern Chile and the rupture area of the 2011 Tohoku earthquake are examples. There are not yet any REEF measurements for Alaska and Cascadia subduction zones, but the occurrence of historical giant earthquakes and the lack of moderate-size events in these regions indicate similarity to southern Chile.

Case 2. Low REEF value (smooth asperity/rupture) and low to moderate $R_C$ (large separation, heterogeneous)

This is the situation in southern Mexico and Middle America. Because of the low fraction of the earthquake slip area ($R_C$), plate coupling is relatively low. The northern Japan to southern Kuril region is in this category. In this case, multiple asperity failure can occasionally happen, as in the large 1843 and 1894 Kushiro-Oki (Hokkaido) and the 1787 Guerrero-Tehuantepec earthquakes. However, these events rupturing across a suite of asperities are relatively rare occurrences due to relatively low plate coupling and a low REEF value.

Case 3. High REEF value (rough asperity/rupture) and high $R_C$ (small separation, uniform)

This is similar to case 1. There is no corresponding example so far; the associated homogeneity of coupling implies smooth rupture over asperities, leading to behavior like in case 1 with a low REEF value.

Case 4. High REEF value (rough asperity/rupture) and low to moderate $R_C$ (large separation, heterogeneous)

This is the case for subduction zones with the observed highest average REEF, such as Colombia–Ecuador–Peru–northern Chile, Solomon Islands, and Sumatra subduction zones. The relatively large separation between rough patches results in heterogeneous coupling. Patch interaction and triggering are more likely to occur than in the low-REEF regions, producing compound events such as the 2007 $M_w$ 8.0 Peru earthquake (*3*). The 1868–1877 Arica and 1906 $M_w$ 8.5 Colombia-Ecuador events are likely to belong to this category. The 2004 Sumatra earthquake started at a large slip patch in the south possibly with a relatively high REEF value, like the 2005 $M_w$ 8.6 Nias earthquake, and this initial rupture was strong enough to coseismically trigger the well-separated patches to the north along the Nicobar and Andaman Islands. Thus, this event also likely belongs to this category. If the separation is too large to cause immediate triggering, then delayed triggering may occur, resulting in distinct doublets such as those in the Solomon Islands (*3*). Of course, other factors such as the evolving stress and strength conditions associated with a particular asperity may cause variability in the rupture behavior, and the triggering can occur coseismically, rather than as a distinct doublet. An example of this is the 2007 $M_w$ 8.1 Solomon Islands event (*3*).

In general, REEF values for earthquakes with dominant slip close to the trench are low (for example, 1994 Java, 2010 Mentawai, and 2011 Tohoku), but occasionally, multiasperity rupture occurs (for example, 2006 Java), giving enhanced REEF.

On the basis of average REEF values and slip patterns, we assign subduction zones and great earthquakes with compound ruptures to the categories of our modified asperity representation shown in Fig. 5. The assignment of each region along the *y* axis is based on slip patch dimensions taken from inverted slip models (*21*). This framework, which combines both rupture zone roughness and triggering, provides a scenario for how different degrees of complexity arise depending on persistent geologic factors and triggering interactions.

Enhanced rupture complexity resulting from multiple asperity failures spreads the range of observed REEF, especially for those subduction zones with high-REEF asperities. Large variations around the average in high-REEF regions suggest that the increase of REEF due to compound rupture in those regions (right cases in Fig. 5) is larger than in those regions with low-REEF failures (left cases in Fig. 5). Magnitude increase due to compound rupture is also larger for high-REEF regions, such as Sumatra and Ecuador-Colombia, compared to low-REEF regions of central Aleutians and Middle America. Because patch interaction depends on the driving stress, the stress state and strength of both triggering and triggered patches, and the history of regional stress variation, the resulting earthquake behavior is noncharacteristic, as observed for the Ecuador-Colombia sequence (*15*). Although there are no direct observations, we suspect that the triggering capability is also higher for regions with high-REEF asperities such as in Ecuador-Colombia, northern Chile, and Sumatra subduction zones, resulting in irregular long-term earthquake sequences. Thus, the combination of $M_w$ and REEF can better represent the span of rupture characteristics of great earthquakes.

REEF provides a new quantitative framework for measuring and categorizing regional variations in rupture characteristics of large earthquakes. Rupture complexity measured by REEF appears to reflect local persistent geological factors that affect rupture dynamics. Those factors could include lithology and temperature, which affect fault friction and dynamic weakening, variation in the presence of fluids and its migration, and geometry of the plate interface. They may be related, in turn, to age and roughness of the subducting seafloor, thickness of sediment cover, convergence rate, or forearc characteristics. They would also affect the heterogeneity of interseismic coupling, resulting in different seismicity patterns. We do not expect simple relations of REEF with large regional geological and tectonic parameters (fig. S10), but dynamical modeling under varying regional conditions may elucidate the fundamental controls on REEF. As we improve our understanding of what local conditions control rupture complexity quantified by REEF in a given region, it may be possible to estimate high-frequency strong ground shaking more precisely for hazard mitigation if the rupture process is hierarchical at varying scales (*29*). REEF measures may then help constrain the fractal dimensions for different hierarchical levels. Connections of REEF with field observations such as geometrical fault structure (*30*) and fault surface roughness (*31*) would help achieve better understanding of earthquake mechanics.

## SUPPLEMENTARY MATERIALS

Supplementary material for this article is available at http://advances.sciencemag.org/cgi/content/full/4/3/eaao4915/DC1

section S1. Uncertainty in estimating seismic moment, source duration, radiated energy, and REEF

section S2. Roughness of the MRF

section S3. Possible geological factors

fig. S1. Map of static stress drop estimates for 119 global large megathrust earthquakes.

fig. S2. Map of seismic moment–scaled cubed source duration for large megathrust events.

fig. S3. Map view of REEF estimates with the total duration assumed to be equal to $2T_c$.

fig. S4. Comparison of radiated energy for magnitude ~7.5 earthquake measured by different methods.

fig. S5. Relative uncertainty estimation for radiated energy $E_R$.

fig. S6. Map view of REEF values and regional average.

## REFERENCES AND NOTES

1. T. Lay, H. Kanamori, An asperity model of large earthquake sequences, in *Earthquake Prediction, An International Review*, D. W. Simpson, P.G. Richards, Eds. (Maurice Ewing Series, AGU, 1981), vol. 4, pp. 579–592.
2. S. P. Nishenko, Circum-Pacific seismic potential: 1989–1999. *Pure Appl. Geophys.* **135**, 169–259 (1991).
3. T. Lay, The surge of great earthquakes from 2004 to 2014. *Earth Planet. Sci. Lett.* **409**, 133–146 (2015).
4. D. Dreger, R. M. Nadeau, A. Chung, Repeating earthquake finite source models: Strong asperities revealed on the San Andreas Fault. *Geophys. Res. Lett.* **34**, L23302 (2007).
5. H. Kawamura, T. Hatano, N. Kato, S. Biswas, B. K. Chakrabarti, Statistical physics of fracture, friction, and earthquakes. *Rev. Mod. Phys.* **84**, 839–884 (2012).
6. A. Heuret, C. P. Conrad, F. Funiciello, S. Lallemand, L. Sandri, Relation between subduction megathrust earthquakes, trench sediment thickness and upper plate strain. *Geophys. Res. Lett.* **39**, L05304 (2012).
7. D. W. Scholl, S. H. Kirby, R. E. von Huene, H. Ryan, R. E. Wells, E. L. Geist, Great (≥Mw8.0) megathrust earthquakes and the subduction of excess sediment and bathymetrically smooth seafloor. *Geosphere* **11**, 236–265 (2015).
8. R. M. Nadeau, L. R. Johnson, Seismological studies at Parkfield VI: Moment release rates and estimates of source parameters for small repeating earthquakes. *Bull. Seism. Soc. Am.* **88**, 790–814 (1998).
9. T. Matsuzawa, T. Igarashi, A. Hasegawa, Characteristic small-earthquake sequence off Sanriku, northeastern Honshu, Japan. *Geophys. Res. Lett.* **29**, 38–1–38-4 (2002).
10. M. Moreno, M. Rosenau, O. Oncken, 2010 Maule earthquake slip correlates with pre-seismic locking of Andean subduction zone. *Nature* **467**, 198–202 (2010).
11. S. Barbot, N. Lapusta, J.-P. Avouac, Under the hood of the earthquake machine: Toward predictive modeling of the seismic cycle. *Science* **336**, 707–710 (2012).
12. C. H. Scholz, Earthquakes and friction laws. *Nature* **391**, 37–42 (1998).
13. G. Plafker, R. Meyer, Uplift history and earthquake recurrence as deduced from marine terraces on Middleton Island, Alaska, in *Proceedings of Conference VI, Methodology for identifying seismic gaps and soon-to-break gaps* (U.S. Geological Survey, Open-File Report 78-943, 1978).
14. M. Cisternas, Unusual geologic evidence of coeval seismic shaking and tsunamis shows variability in earthquake size and recurrence in the area of the giant 1960 Chile earthquake. *Mar. Geol.* **385**, 101–113 (2017).
15. L. Ye, H. Kanamori, J. P. Avouac, L. Li, K. F. Cheung, T. Lay, The 16 April 2016, $M_W$ 7.8 ($M_S$ 7.5) Ecuador earthquake: A quasi-repeat of the 1942 $M_S$ 7.5 earthquake and partial re-rupture of the 1906 $M_S$ 8.6 Colombia–Ecuador earthquake. *Earth Planet. Sci. Lett.* **454**, 248–258 (2016).
16. Y. Tanioka, K. Hirata, R. Hino, T. Kanazawa, Slip distribution of the 2003 Tokachi-oki earthquake estimated from tsunami waveform inversion. *Earth, Planets Space* **56**, 373–376 (2004).
17. K. Satake, Geological and historical evidence of irregular recurrent earthquakes in Japan. *Phil. Trans. R. Soc. A* **373**, 10.1098/rsta.2014.0375 (2015).
18. L. Ye, T. Lay, H. Kanamori, The Sanriku-Oki low-seismicity region on the northern margin of the great 2011 Tohoku-Oki earthquake rupture. *J. Geophys. Res.* **117**, B02305 (2012).
19. N. Uchida, K. Shimamura, T. Matsuzawa, T. Okada, Postseismic response of repeating earthquakes around the 2011 Tohoku-oki earthquake: Moment increases due to the fast loading rate. *J. Geophys. Res.* **120**, 259–274 (2015).
20. P. Dublanchet, P. Bernard, P. Favreau, Interactions and triggering in a 3-D rate-and-state asperity model. *J. Geophys. Res.* **118**, 2225–2245 (2013).
21. L. Ye, T. Lay, H. Kanamori, L. Rivera, Rupture characteristics of major and great ($Mw \geq 7.0$) megathrust earthquakes from 1990 to 2015: 1. Source parameter scaling relationships. *J. Geophys. Res.* **121**, 826–844 (2016).
22. H. Kanamori, L. Rivera, Static and dynamic scaling relations for earthquakes and their implications for rupture speed and stress drop. *Bull. Seism. Soc. Am.* **94**, 314–319 (2004).
23. C. J. Ammon, H. Kanamori, T. Lay, A. A. Velasco, The 17 July 2006 Java tsunami earthquake. *Geophys. Res. Lett.* **33**, L24308 (2006).
24. L. Ye, T. Lay, H. Kanamori, Large earthquake rupture process variations on the Middle America megathrust. *Earth Planet. Sci. Lett.* **381**, 147–155 (2013).
25. H. Perfettini, J.-P. Avouac, H. Tavera, A. Kositsky, J.-M. Nocquet, F. Bondoux, M. Chlieh, A. Sladen, L. Audin, D. L. Farber, P. Soler, Seismic and aseismic slip on the Central Peru megathrust. *Nature* **465**, 78–81 (2010).
26. M. Métois, C. Vigny, A. Socquet, Interseismic coupling, megathrust earthquakes and seismic swarms along the Chilean subduction zone (38°–18°S). *Pure Appl. Geophys.* **173**, 1431–1449 (2016).
27. C. J. Ammon, H. Kanamori, T. Lay, A great earthquake doublet and seismic stress transfer cycle in the central Kuril islands. *Nature* **451**, 561–565 (2008).
28. S. Y. Schwartz, Noncharacteristic behavior and complex recurrence of large subduction zone earthquakes. *J. Geophys. Res.* **104**, 23111–23125 (1999).
29. Y. Fukao, M. Furumoto, Hierarchy in earthquake size distribution. *Phys. Earth Planet. Inter.* **37**, 149–168 (1985).
30. C. W. D. Milliner, C. Sammis, A. A. Allam, J. F. Dolan, J. Hollingsworth, S. Leprince, F. Ayoub, Resolving fine-scale heterogeneity of co-seismic slip and the relation to fault structure. *Sci. Rep.* **6**, 27201 (2016).
31. E. E. Brodsky, J. D. Kirkpatrick, T. Candela, Constraints from fault roughness on the scale-dependent strength of rocks. *Geology* **44**, 19–22 (2016).
32. X. Pérez-Campos, S. K. Singh, G. C. Beroza, Reconciling teleseismic and regional estimates of seismic energy. *Bull. Seismol. Soc. Am.* **93**, 2123–2130 (2003).
33. L. Ye, T. Lay, H. Kanamori, Ground shaking and seismic source spectra for large earthquakes around the megathrust fault offshore of northeastern Honshu, Japan. *Bull. Seismol. Soc. Am.* **103**, 1221–1241 (2013).
34. J. Boatwright, G. L. Choy, Teleseismic estimates of the energy radiated by shallow earthquakes. *J. Geophys. Res.* **91**, 2095–2112 (1986).
35. J. A. Convers, A. V. Newman, Global evaluation of large earthquake energy from 1997 through mid-2010. *J. Geophys. Res.* **116**, B08304 (2011).
36. H. Jeffreys, The Pamir earthquake of 1911 February 18, in relation to the depth of earthquake foci. *Mon. Not. R. Astron. Soc.* **1**, 22–31 (1923).
37. B. Gutenberg, C. F. Richter, Earthquake magnitude, intensity, energy, and acceleration (second paper). *Bull. Seism. Soc. Am.* **46**, 105–145 (1956).
38. L. Ruff, H. Kanamori, Seismicity and the subduction process. *Phys. Earth Planet. Inter.* **23**, 240–252 (1980).
39. D. Bassett, A. B. Watts, Gravity anomalies, crustal structure, and seismicity at subduction zones: 1. Seafloor roughness and subducting relief. *Geochem. Geophys. Geosyst.* **16**, 1508–1540 (2015).
40. C. H. Scholz, J. Campos, The seismic coupling of subduction zones revisited. *J. Geophys. Res.* **117**, B05310 (2012).
41. Q. Bletery, A. M. Thomas, A. W. Rempel, L. Karlstrom, A. Sladen, A. L. De Barros, Mega-earthquakes rupture flat megathrusts. *Science* **354**, 1027–1031 (2016).
42. K. Berryman, L. Wallace, G. Hayes, P. Bird, K. Wang, R. Basili, T. Lay, M. Pagani, R. Stein, T. Sagiya, C. Rubin, S. Barreintos, C. Kreemer, N. Litchfield, M. Stirling, K. Gledhill, K. Haller, C. Costa, The GEM Faulted Earth Subduction Interface Characterisation Project, Version 2.0 (2015).
43. E. M. Syracuse, P. E. Van Keken, G. A. Abers, The global range of subduction zone thermal models. *Phys. Earth Planet. Inter.* **183**, 73–90 (2010).

**Acknowledgments:** We thank J. P. Avouac, N. Lapusta, L. Rivera, R. Bürgmann, S. Ide, T. Hanks, several anonymous reviewers, and the editor G. Beroza for constructive suggestions and comments on this work. **Funding:** This study was supported by a National Natural Science Foundation of China grant (no. 41590893) and the joint program of the Chinese Academy of Sciences and the National Natural Science Foundation of China (no. L1624024) to L.Y. and an NSF grant to T.L. (no. EAR1245717). **Author contributions:** L.Y. and H.K. conceived the normalization by a reference energy model. L.Y., H.K., and T.L. conducted the analysis and wrote the paper collectively. **Competing interests:** The authors declare that they have no competing interests. **Data and materials availability:** Source parameters of seismic moment, rupture duration, radiated energy, and stress drop for each earthquake are from the study of Ye *et al.* (*21*), available from the online website https://sites.google.com/site/linglingye001/earthquakes/slip-models. All data needed to evaluate the conclusions in the paper are present in the paper and/or the Supplementary Materials. Additional data related to this paper may be requested from the authors.

Submitted 26 July 2017
Accepted 8 February 2018
Published 21 March 2018
10.1126/sciadv.aao4915

**Citation:** L. Ye, H. Kanamori, T. Lay, Global variations of large megathrust earthquake rupture characteristics. *Sci. Adv.* **4**, eaao4915 (2018).

Science Advances

AAAS

advances.sciencemag.org/cgi/content/full/4/3/eaao4915/DC1

# Supplementary Materials for

## Global variations of large megathrust earthquake rupture characteristics

Lingling Ye, Hiroo Kanamori, Thorne Lay

Published 21 March 2018, *Sci. Adv.* **4**, eaao4915 (2018)
DOI: 10.1126/sciadv.aao4915

**This PDF file includes:**

**section S1. Uncertainty in estimating seismic moment, source duration, radiated energy, and REEF**

Seismic moment is the most robust measurement of earthquakes determined from long-period observations, so we neglect its contribution to the uncertainty of *REEF* estimates.

The total source duration $T$ used in this study is defined by the time when the moment time function (time integral of MRF from finite-fault models[21]) reaches ~95% of the final value. Total duration measures can be influenced by water reverberations and late scattered waves. We ignore very weak tails in MRFs as these are likely to be artifacts of inaccurate modeling of the coda in combination with the positivity constraint used in the slip inversion. The uncertainty in source duration estimated this way is ~10% for large earthquakes; some M7 events might have larger uncertainty of ~20%. A 10% variation of $T$ results in a 30% variation in estimated $E_{R\_min}$ thus the duration uncertainty can affect the *REEF* estimates significantly. Because the definition of $T$ described above is somewhat subjective, we consider another definition of $T$ using $T_c$, the MRF centroid delay time measured from the origin time. $T_c$ estimated from our MRFs of finite-fault slip models are consistent with those determined by the inversion of long-period waves as provided by the global Centroid Moment Tensor catalog and Wphase inversions[21]. The advantage of using this definition is that $T_c$ can be determined objectively without any subjective judgement and $2T_c$ gives a reasonable estimate of $T$. However, if the MRF has a long tail or slow rise time, $2T_c$ underestimates or overestimates $T$, respectively. As shown in fig. S3, the *REEF* values estimated with $T$=$2T_c$ show similar regional patterns, with only minor differences, to those found using our measures of total durations (Fig. 4). Although we present the *REEF* values using the measured total duration in this study, use of a different definition of $T$ would not significantly affect our conclusions.

We estimate the radiated energy by combining the moment-rate spectrum (MRS) estimated from finite-fault inversion at low frequency (0-0.05 Hz) and the average P-wave displacement spectrum at high frequency (0.05 – 1 Hz) (ref. 21). The displacement

spectrum is corrected for attenuation, radiation pattern and surface reflection. We use the model of Perez-Campos et al.[32] for the attenuation correction[33]. For correction of the radiation pattern and surface reflection, we follow the method of Boatwright and Choy[34], in which the effect of surface reflection is only approximately accounted for. To make sure that this correction is sufficiently accurate for our purpose we compare the P-wave displacement spectrum with that from MRS derived from slip inversion at the cross-over frequency, 0.05Hz. The finite-fault inversion accounts for the effect of surface reflections.

The radiated energy obtained from the broadband spectrum over the 0-1 Hz band accounts for most radiated energy (> ~95% for the assumption that the high-frequency spectrum has the fall-off slope of -2) for $M_W \geq 7$ earthquakes. However, our radiated energy estimates, as well as those from other studies, do not fully account for finite source effects, free surface effects, and scattering of wave propagation. Thus, we cannot rigorously estimate absolute errors in energy estimation. Despite those limitations, with the recent availability of extensive global broadband seismic recordings, the measurement accuracy of radiated energy has been significantly improved over the last century (fig. S4).

As we focus on relative *REEF* values, only the relative uncertainty in radiated energy is needed. Out of the 119 total events in this study, we consider 90 earthquakes which have three independent estimates of radiated energy from USGS-NEIC, IRIS, and our previous study (ref., 21), noted as $E_R^{(USGS\text{-}NEIC)}$, $E_R^{(IRIS)}$ and $E_R^{(YKLR)}$, respectively. Figure S5a shows the ratio $E_R^{(USGS\text{-}NEIC)}/E_R^{(YKLR)}$ and $E_R^{(IRIS)}/E_R^{(YKLR)}$ as a function of magnitude. No obvious trend with magnitude is seen but $E_R^{(\mathrm{IRIS})}$ and $E_R^{(\mathrm{USGS\text{-}NEIC})}$ are about 83% and 42% of $E_R^{(YKLR)}$. Thus, the difference between the estimates from these data sets is probably due to small differences in time windows, frequency bands, weighting of *P* and *S* radiation, and velocity structures used in the calculations. Then, as a measure of relative uncertainty of energy estimate for each event, we calculate the geometric mean and standard deviation of $E_R^{(IRIS)}/0.83$, $E_R^{(USGS\text{-}NEIC)}/0.42$ and $E_R^{(YKLR)}$ for each event (fig. S5b and S5c). Except for a few large outliers, standard deviations range from ~1.2 to ~1.8

with an average of ~1.45. We thus infer that the uncertainty of relative radiated energy estimates for large megathrust earthquakes is about 45%.

With uncertainties from rupture duration cubed (~30%) and radiated energy (~45%), the uncertainty of relative *REEF* values is about a factor of 2. There is greater uncertainty in absolute values of radiated energy, so it is important to compare *REEF* values that use consistently estimated values of $E_R$. Regionally consistent behavior that emerges from the measurements is subject to even less uncertainty. In the categorization based on regional average *REEF* values in Fig. 5, the low-*REEF* failures have average values of ~5-10 with relatively small variation, less than a factor of ~2, whereas the high-*REEF* failures have average values of ~20-50 with large variation (Figs. 4, S6). Japan, S. Kurils and South Sumatra have medium average *REEF* values. Low and high *REEF* regions with enough samples have well-separated ranges of *REEF* values (Figs. 4, S6), justifying the basic categorization.

**section S2. Roughness of the MRF**

One can also represent rupture complexity by the roughness of estimated moment-rate functions (MRFs) derived from finite-fault inversion for large events[21]. We compute γ by

$$\gamma = \frac{\int_0^T \ddot{M}(t)^2\,dt}{\int_0^T \dot{u}(t)^2\,dt} = \frac{E_R^M}{E_{R\_\min}}, \qquad (4)$$

and call it the MRF roughness. Here, $\ddot{M}(t)$ and $\dot{u}(t)$ are time derivatives of the observed and the parabolic moment-rate functions respectively. $E_R{}^M$ is the radiated energy estimated from an observed moment-rate function determined from finite-fault inversion. Note that $E_R{}^M$ is different from the broad-band radiated energy, $E_R$. Since high-frequency signals are filtered out as a result of limited knowledge of small-scale Earth structure and simplicity of model parameterizations used for inverting teleseismic data, the estimated

MRF is smoothed and depleted in high-frequency components. This is true for both point-source MRFs estimated by deconvolution methods and MRFs from finite-fault modeling. In contrast, the $E_R$ measurement captures the total radiated energy more completely by the virtue of how the propagation effects are handled. As shown in fig. S7, most *REEF* values are larger than γ for a given event, because of the missing high-frequency energy in $E_R^M$. The difference between *REEF* and γ tends to increase as the magnitude decreases, because the high-frequency components are more important for smaller events (fig. S8). Figure S9 shows all MRFs with values of *REEF* ($E_R/E_{R\_min}$) and γ.

**section S3. Possible geological factors**

Many studies have explored the influence of subduction zone parameters on great earthquakes globally. Early studies (e.g., ref. 38) in the 1980s found that great earthquakes tend to occur in regions with relatively young subducting lithosphere and high plate convergence rate. This hypothesis has been challenged by the occurrence of the 2011 Tohoku earthquake associated with subduction of an old plate. With greater spatial sampling of subduction zone properties, correlations between maximum earthquake size and a variety of geological and tectonic parameters, such as subducted sediment thickness[6,7], seamount or seafloor roughness[39], seismic coupling[40], gravity anomaly[27], and slab dip angle[41] have been examined.

To explore what controls rupture complexity (rather than just earthquake size), we examine correlations of these factors with *REEF* in fig. S10. There is no clear correlation between *REEF* and subduction-zone parameters. Investigations with more global samples accompanied by dynamic modeling under varying regional conditions may elucidate the fundamental controls on rupture complexity.

**table S1. Asperity size, spacing, and earthquake sizes for the modified asperity representation (Fig. 5).**

| # of asperities | *R* (total asperity area/Total area) | *r* (single asperity area/total area) | *L* (2D inter-asperity spacing (1D)) | $M_W$ for single asperity rupture | $M_W$ for rupture of all asperities | $M_W$ for all asperity rupture with excess slip* |
|---|---|---|---|---|---|---|
| **1** | **1** | **1** | **0 (0)** | **9.50** | **9.50** | **9.50** |
| **2** | **1/2** | **1/4** | **1/2 (1/4)** | **8.60** | **8.80** | **9.10** |
| **3** | **1/3** | **1/9** | $\sqrt{2}/3$ (2/9) | **8.07** | **8.39** | **8.69** |
| **4** | **1/4** | **1/16** | $\sqrt{3}/4$ **(3/16)** | **7.69** | **8.10** | **8.40** |

*** We assumed that seismic moment for compound rupture is three times larger than the sum of seismic moment of all single asperity ruptures, as observed for the Ecuador-Colombia large earthquake sequence[15].**

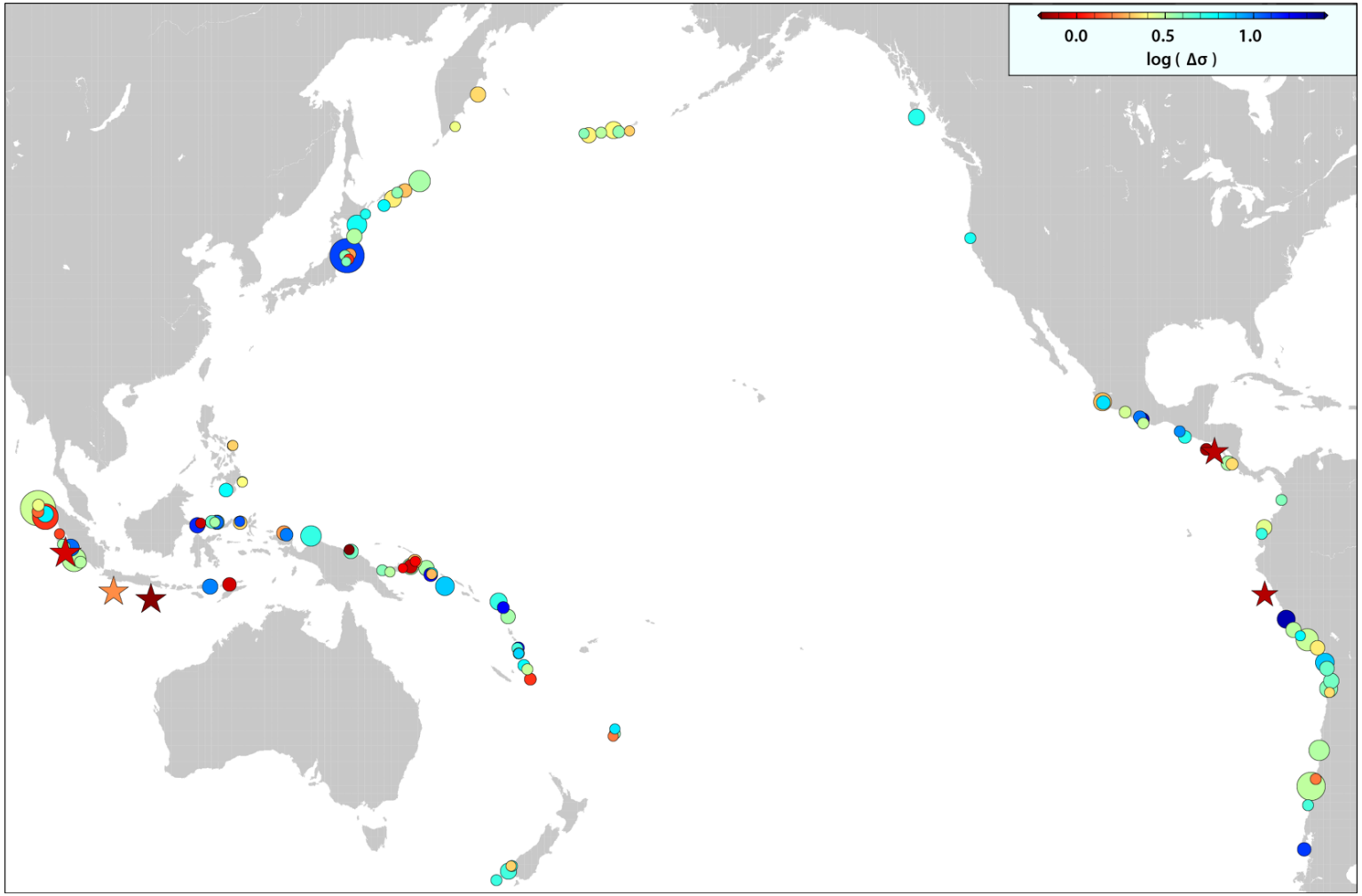


**fig. S1. Map of static stress drop estimates for 119 global large megathrust earthquakes.** Each static stress drop is determined from a finite-fault slip distribution[21] with a unit of MPa. Stars indicate large tsunami earthquakes. Symbol sizes scale with earthquake magnitude.

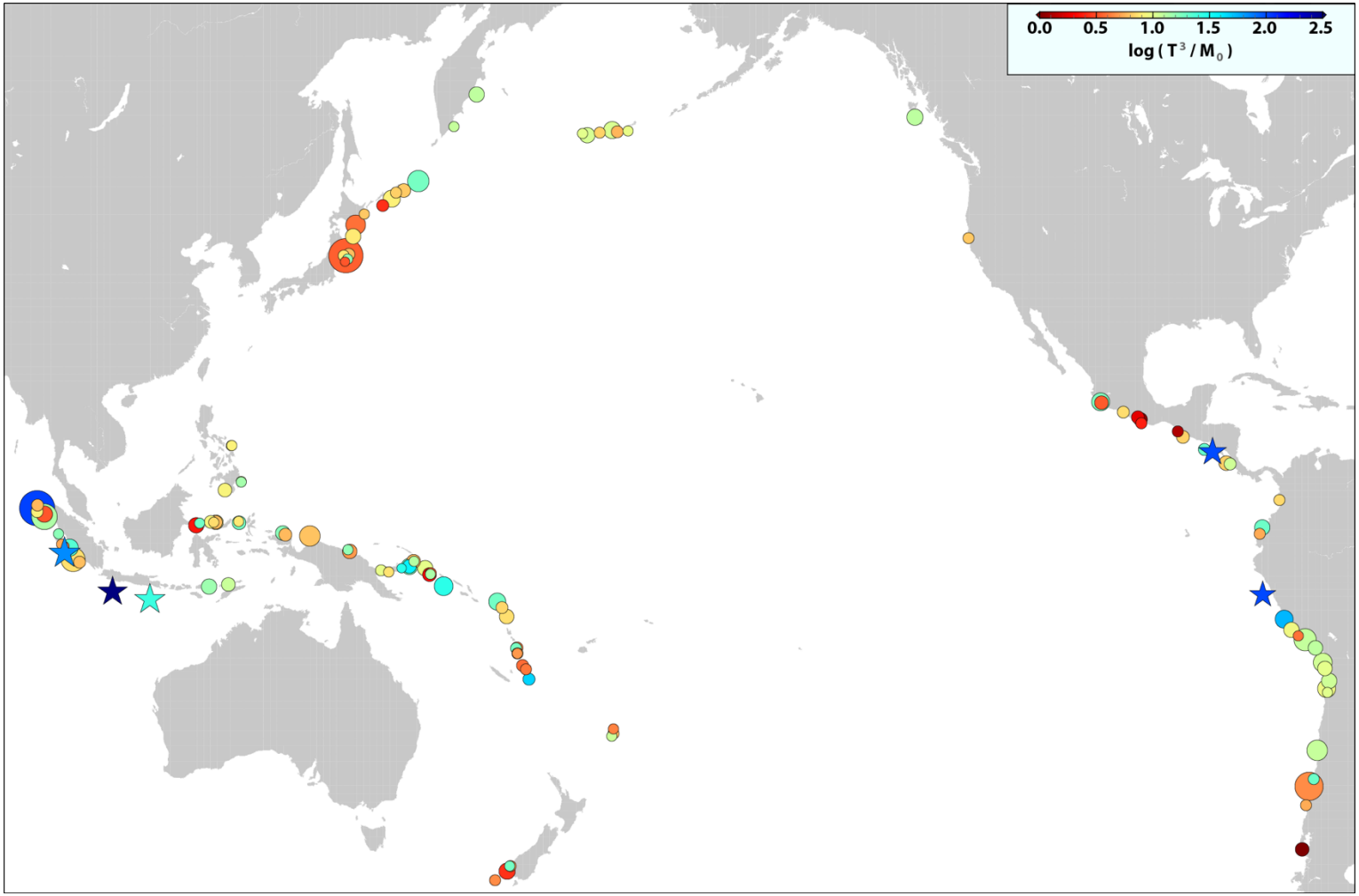


**fig. S2. Map of seismic moment–scaled cubed source duration for large megathrust events.** Stars indicate large tsunami earthquakes. Symbol sizes scale with earthquake magnitude.

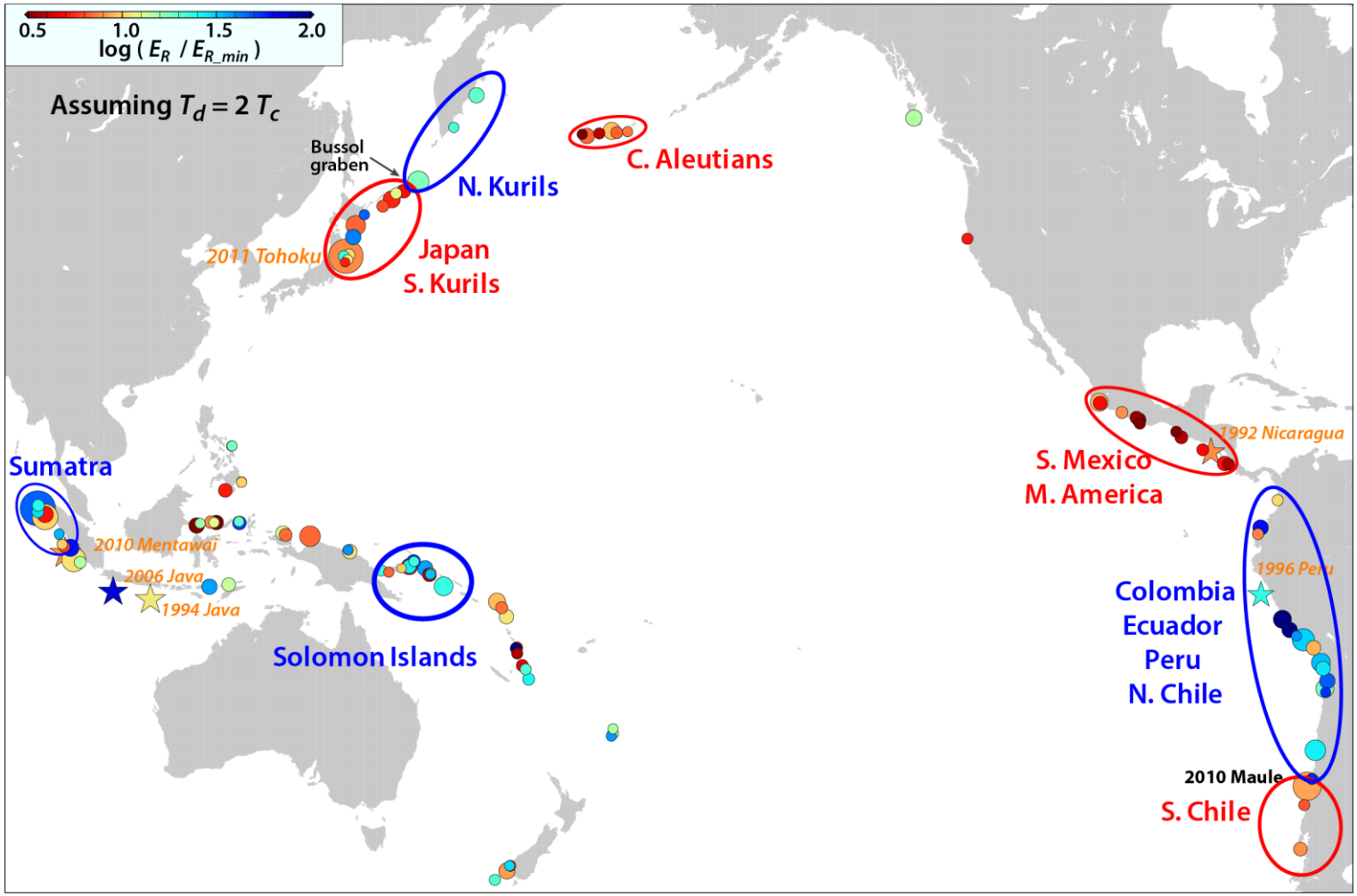


**fig. S3. Map view of REEF estimates with the total duration assumed to be equal to $2T_c$.** Earthquakes are color-coded by the corresponding *REEF* values in $\log_{10}$ scale. Symbol sizes scale with earthquake magnitude. It shows similar regional *REEF* variations to those in Figure 4, suggesting relative stable estimate of *REEF* using the measured total duration.

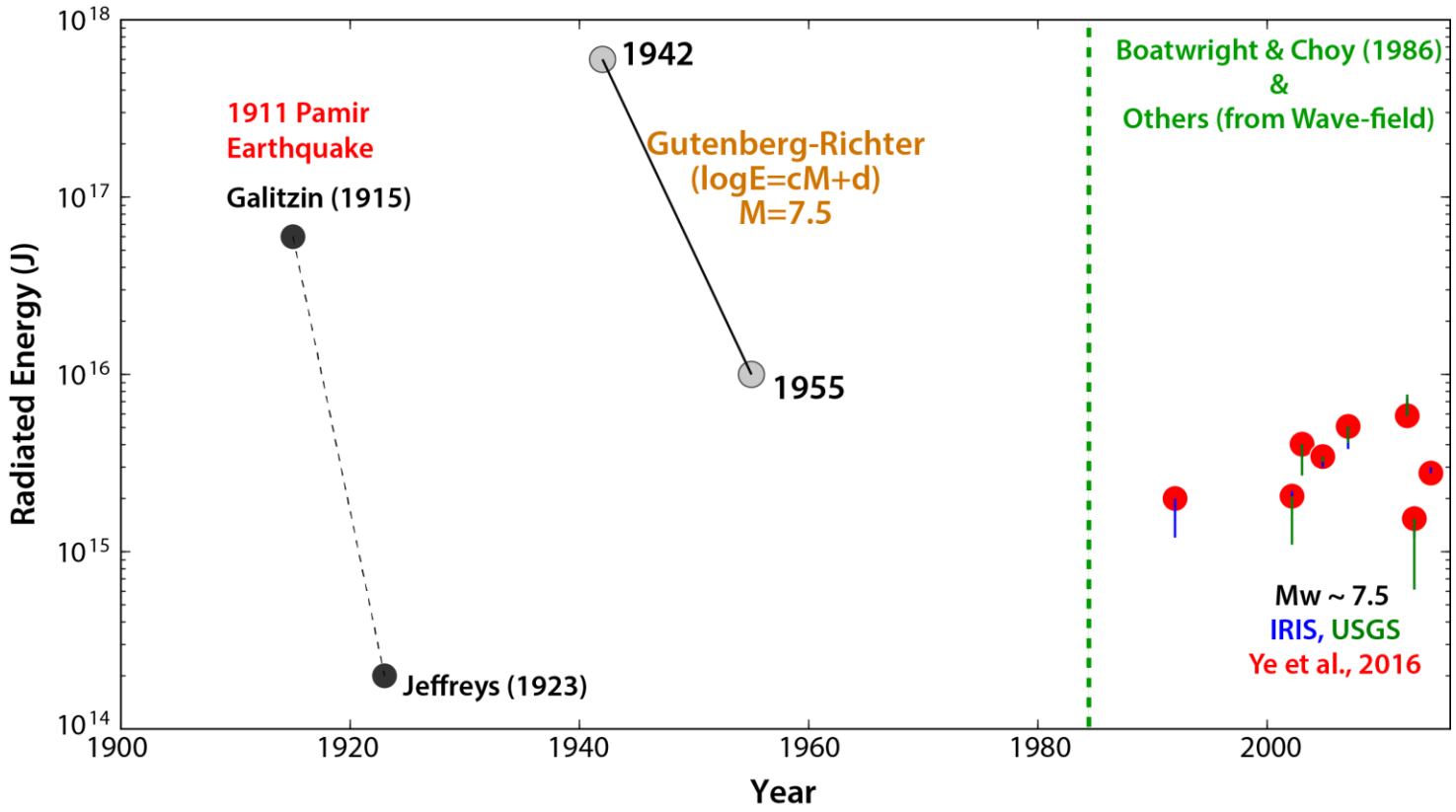


**fig. S4. Comparison of radiated energy for magnitude ~7.5 earthquake measured by different methods.** For the 1911 Pamir earthquake, radiated energy was measured by Galitzin in 1915 and Jeffrey in 1923[36]. There are more than 2 orders of magnitude discrepancy between their results because of different methods. Gutenberg and Richter updated their empirical relations for earthquake magnitude and radiated energy estimates in 1942 and 1956[37], which ends up ~1.5 orders of magnitude difference in the radiated energy for M ~7.5 earthquakes. Since 1990 when the broadband seismic data has been openly available, various groups, such as Ye et al.[21] (red dots), IRIS based on Convers and Newman[35] (different from Ye et al.'s result by blue bars), and USGS based on Boatwright and Choy[34] (different from Ye et al.'s result by green bars), have calculated radiated energy for large earthquake. The right-hand side of the figure compares those results for all *Mw* ~7.5 megathrust earthquakes from 1990 – 2016 with x-axis showing earthquake's occurrence time. With the broadband seismic data and improved wave-field methods, the discrepancy between results from different groups using different methods is within a factor of ~2.

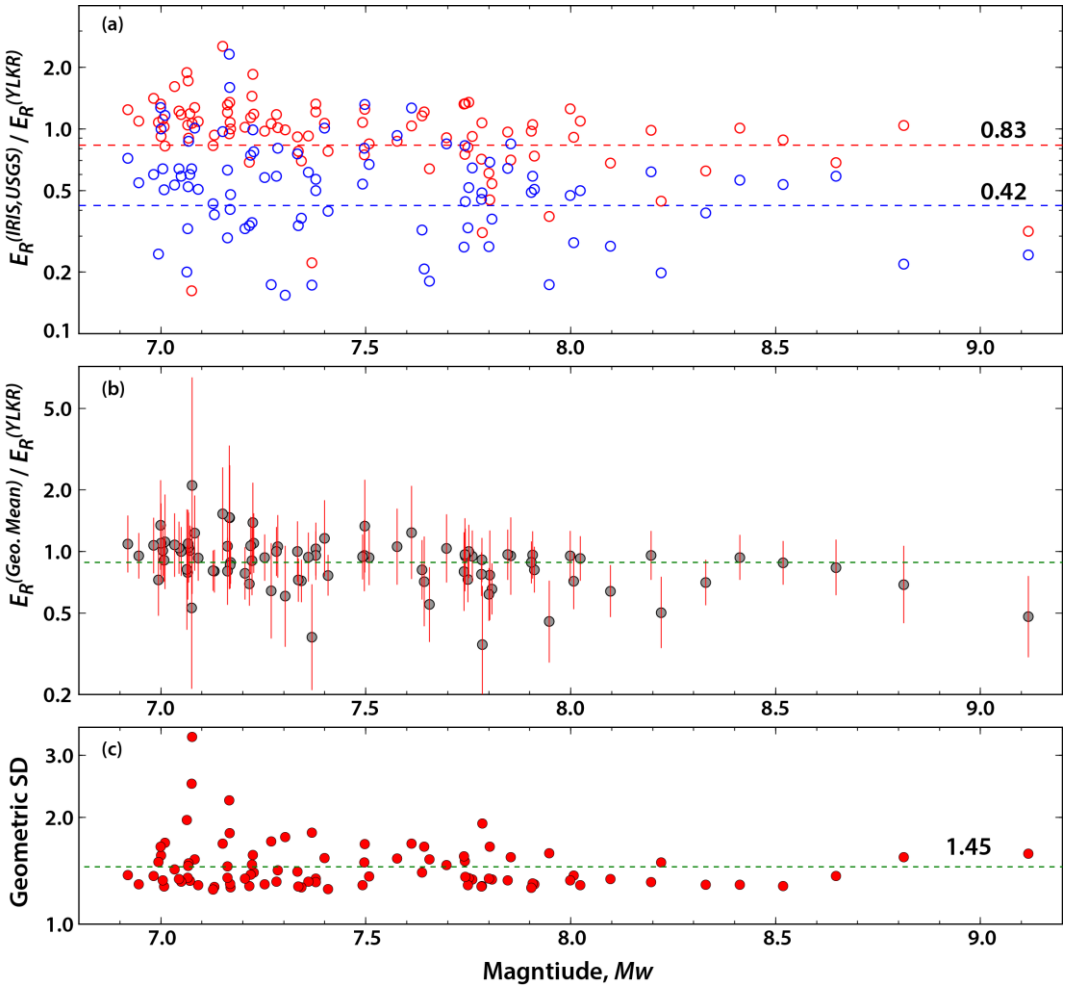


**fig. S5. Relative uncertainty estimation for radiated energy $E_R$.** (a) Ratios of radiated energy estimates for 90 earthquakes from IRIS[35] (red dots) and from USGS-NEIC[34] (blue dots) to our results[21] ($E_R^{(YLKR)}$), plotted against earthquake magnitude. On average, $E_R^{(IRIS)}$ and $E_R^{(USGS\text{-}NEIC)}$ are 83% and 42% of $E_R^{(YLKR)}$. (b) Geometric mean values of $E_R^{(IRIS)}$/0.83 and $E_R^{(USGS\text{-}NEIC)}$/0.42 and $E_R^{(YLKR)}$, normalized by $E_R^{(YLKR)}$, plotted against earthquake magnitude. The red bars show geometric standard deviations for the three estimates of each event. (c) Geometric standard deviations plotted against earthquake magnitude with an average of 1.45.

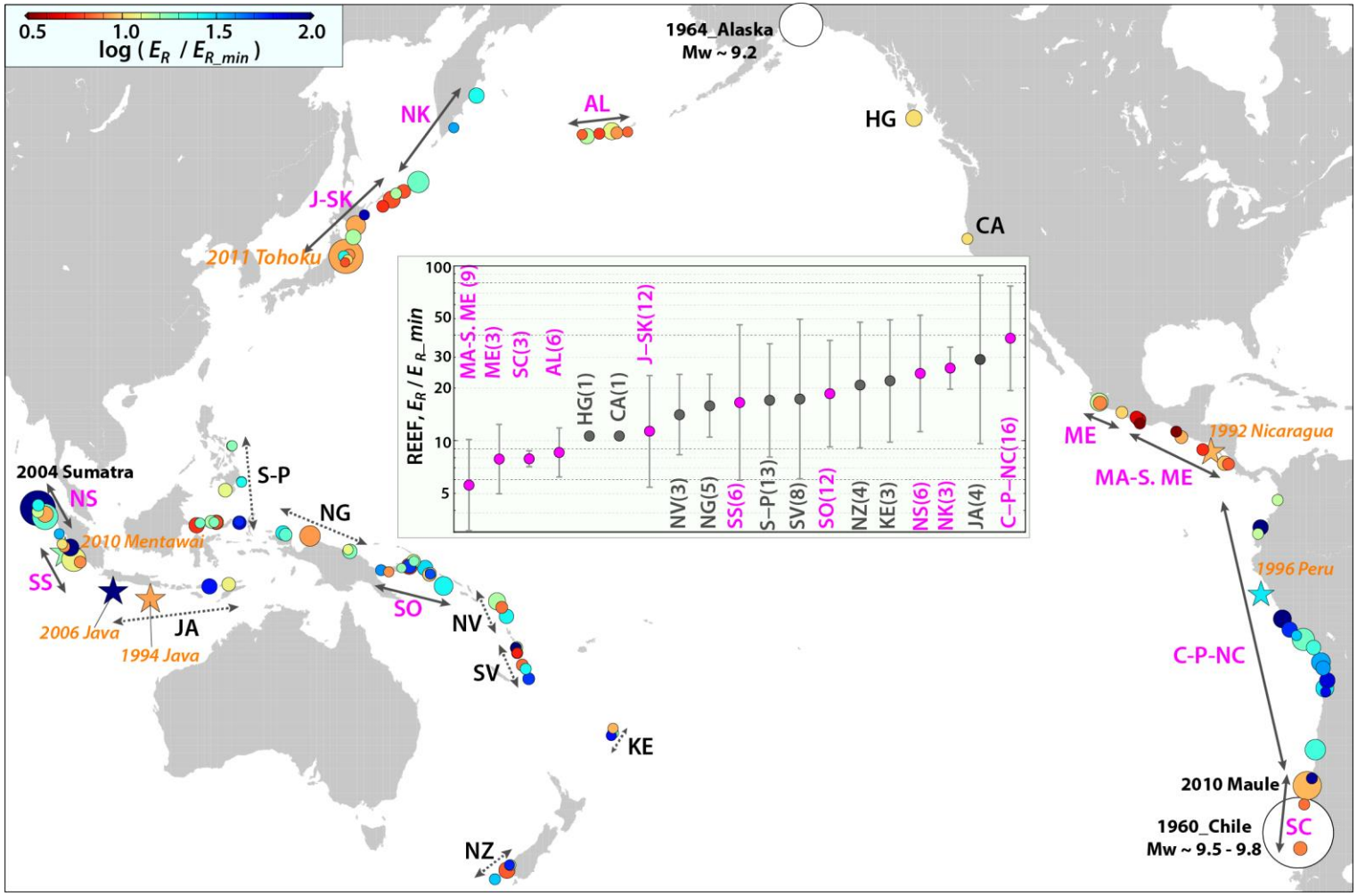


**fig. S6. Map view of REEF values and regional average.** Groups of events in different subduction zones are indicated by the initials and arrows. Stars are for large tsunami earthquakes. Symbols scale with earthquake magnitude. The insert figure shows regional logarithmic average *REEF* values arranged in ascending order, with standard deviation (bars) and number of events. Purple labeling indicates areas with better sampling for the regional average. Note systematic values for some regions as shown in Fig. 4, such as high-*REEF* at Colombia-Ecuador-Peru-N. Chile, N. Kurils, Solomon Islands and Sumatra, and low-*REEF* at Mexico-M. America, S. Chile, N. Japan-S. Kurils, and C. Aleutians.

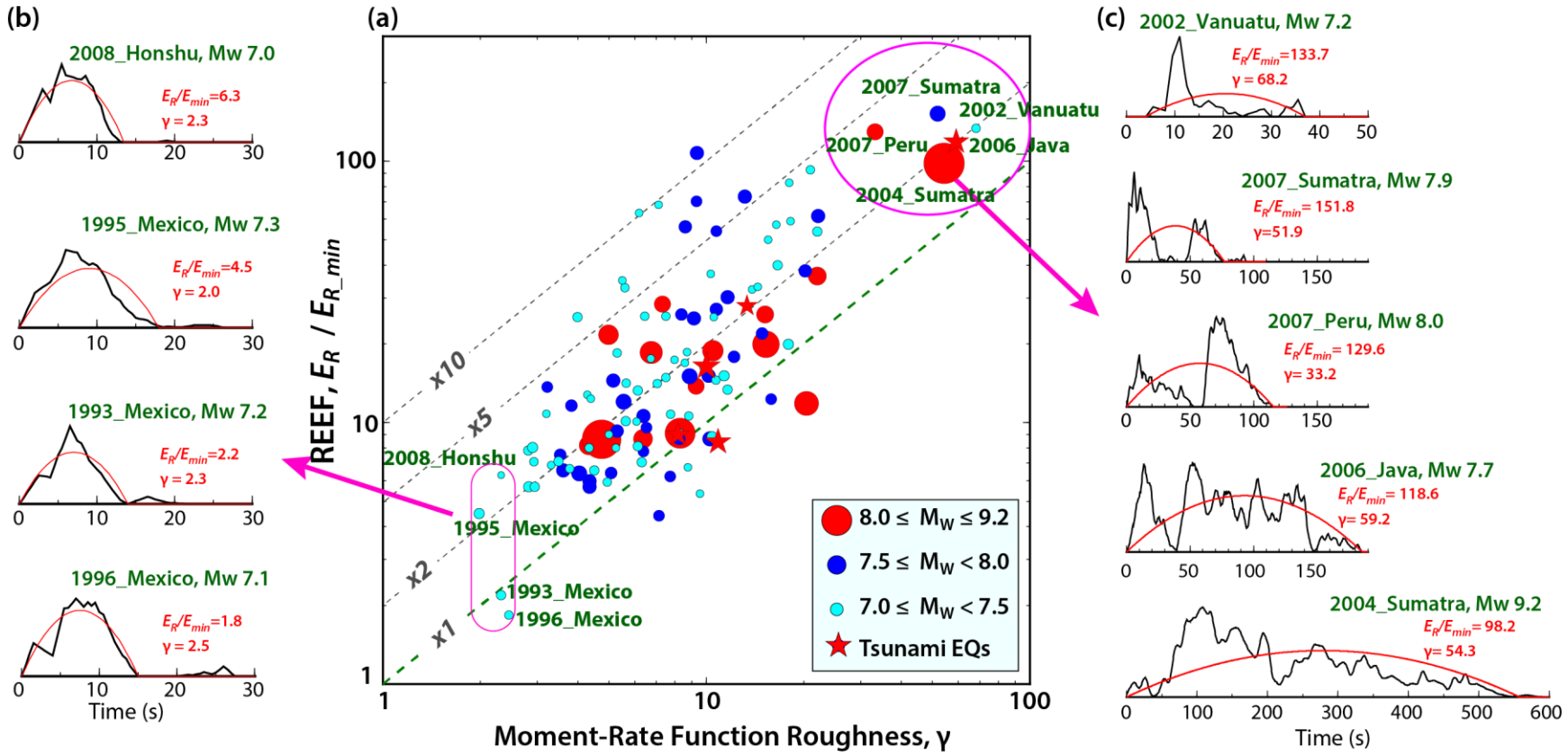


**fig. S7. REEF versus MRF complexity, γ.** (a) *REEF* and $\gamma$ for 119 large megathrust earthquakes. The dashed green line shows equal *REEF* and $\gamma$, and three dashed gray lines show that *REEF* are 2, 5, and 10 times larger than $\gamma$ respectively. MRF (black) and corresponding MRF for $E_{R\_min}$ (red) for earthquakes with low *REEF* and $\gamma$ associated with smooth rupture and with large *REEF* and $\gamma$ associated with complex rupture are shown at (b) and (c) respectively. *REEF* and $\gamma$ correlated with each other, but there is a substantial spread in *REEF* for similar values of $\gamma$.

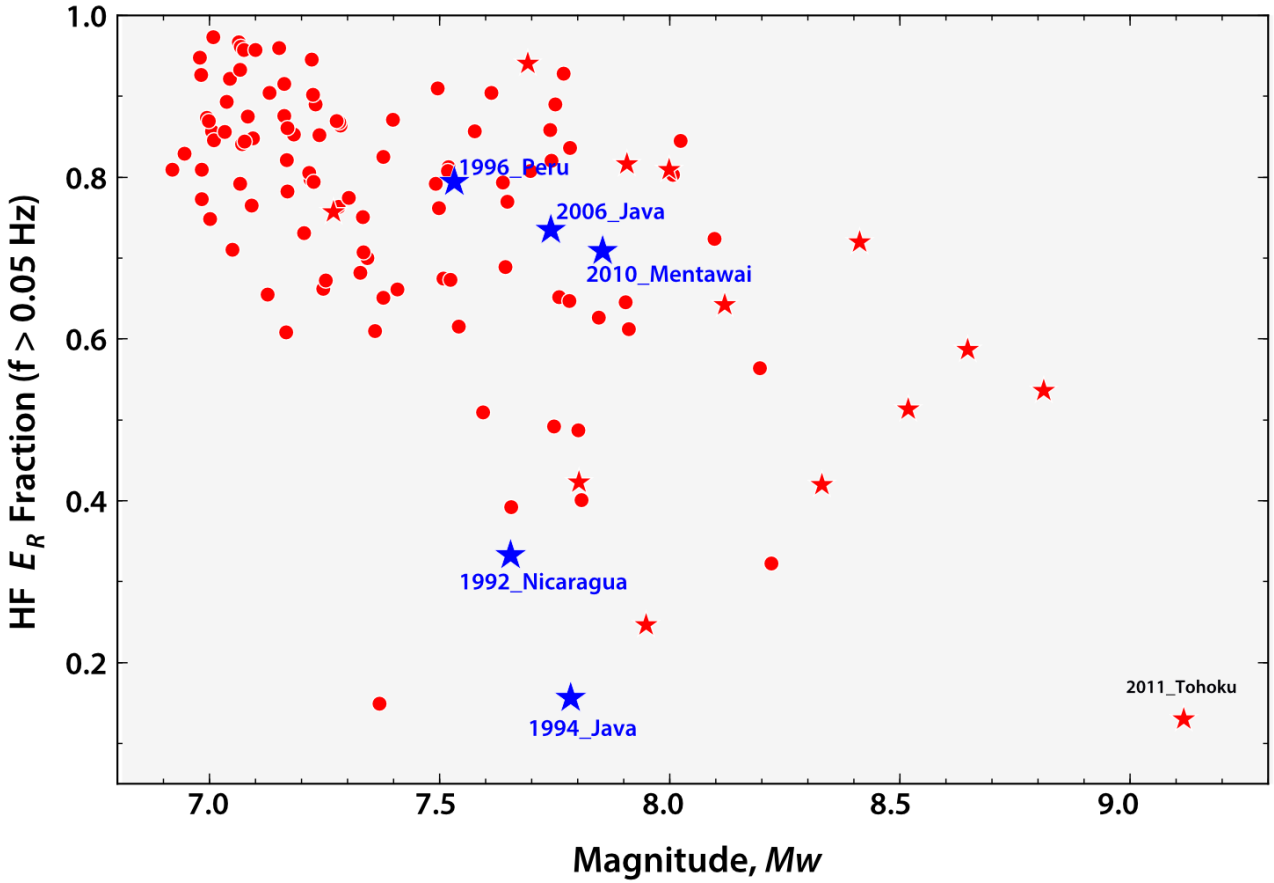


**fig. S8. Fraction of high-frequency (*f* > 0.05 Hz) radiated energy plotted with earthquake magnitude.** Detailed seismic radiated energy measurement procedures are fully documented in Ye et al. (21). Stars and circles show events with and without constraints on rupture speed and source dimensions, respectively. Five large tsunami earthquakes are highlighted in blue. For most M7+ megathrust earthquakes, there is more radiated energy in the frequency range of 0.05-1 Hz than that at lower frequency, except for tsunami earthquakes and giant earthquakes.

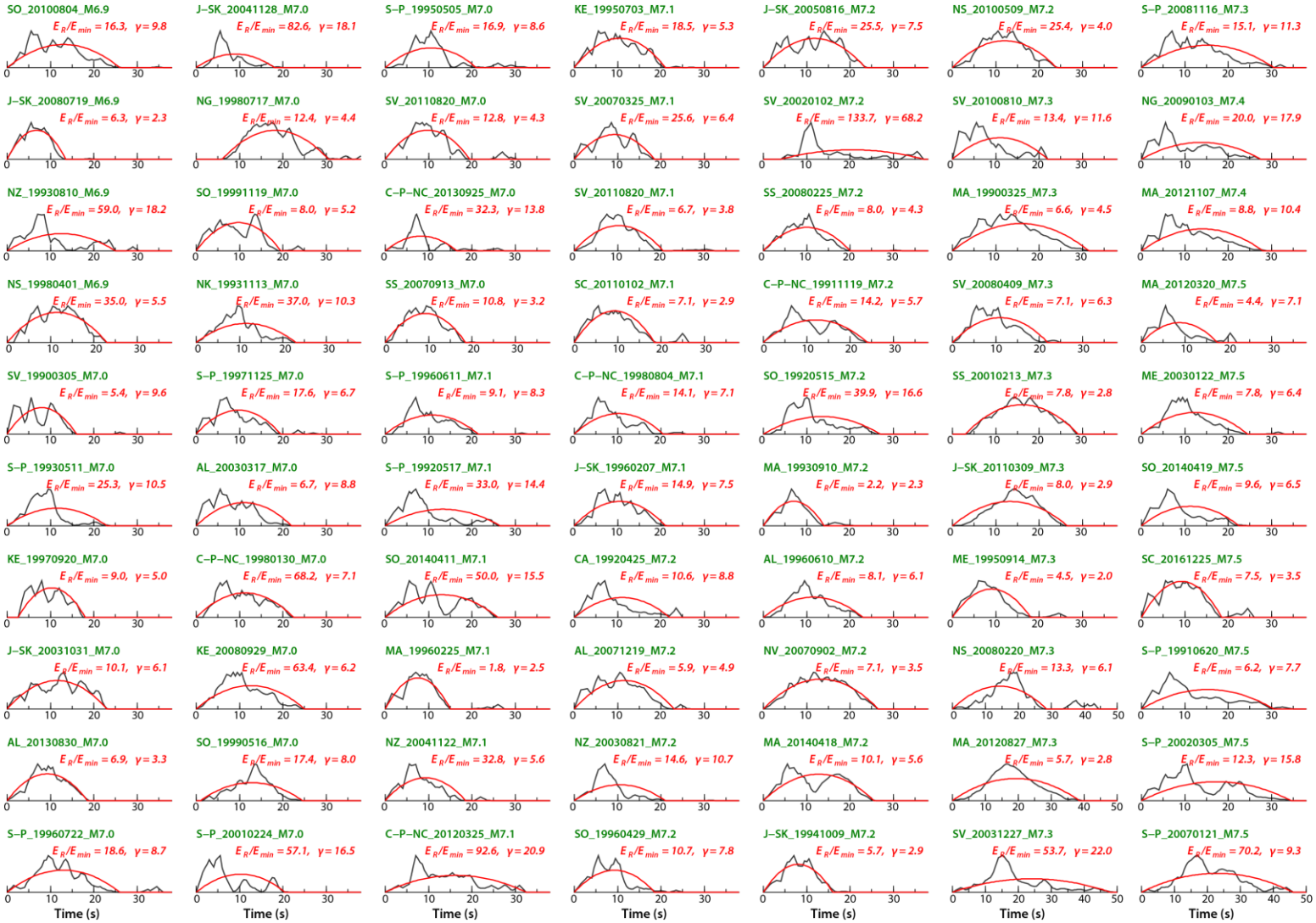


**fig. S9. MRF (black) and corresponding minimum $E_R$ MRF (red) for 119 global large megathrust earthquakes.** The label of each event starts with regional code (fig. S8), occurrence date and magnitude ($M_W$). The *REEF* ($E_R/E_{min}$) and MRF complexity, γ, are marked in red. Earthquakes are listed in ascending order of magnitude.

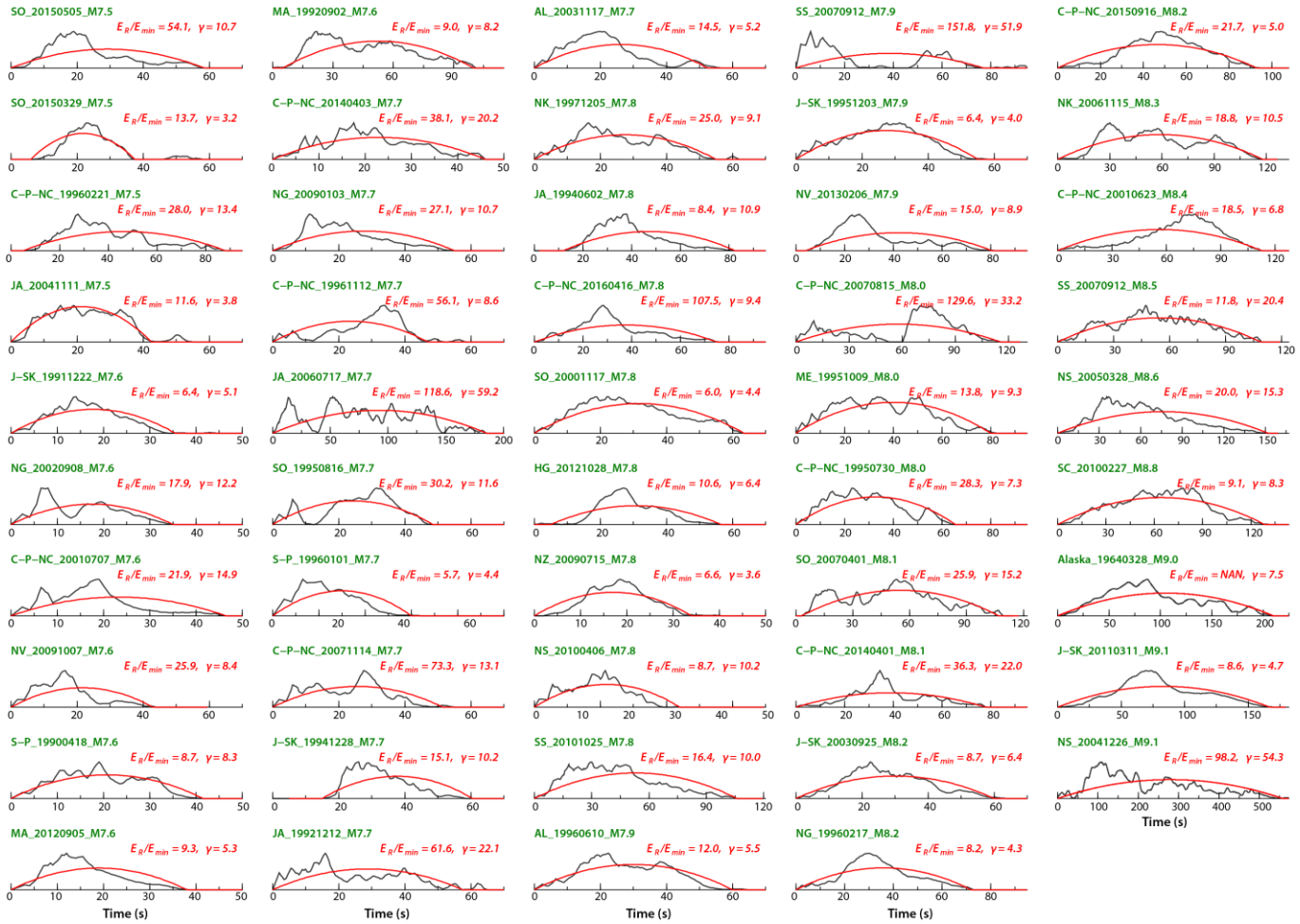


**fig. S9. Continued.**

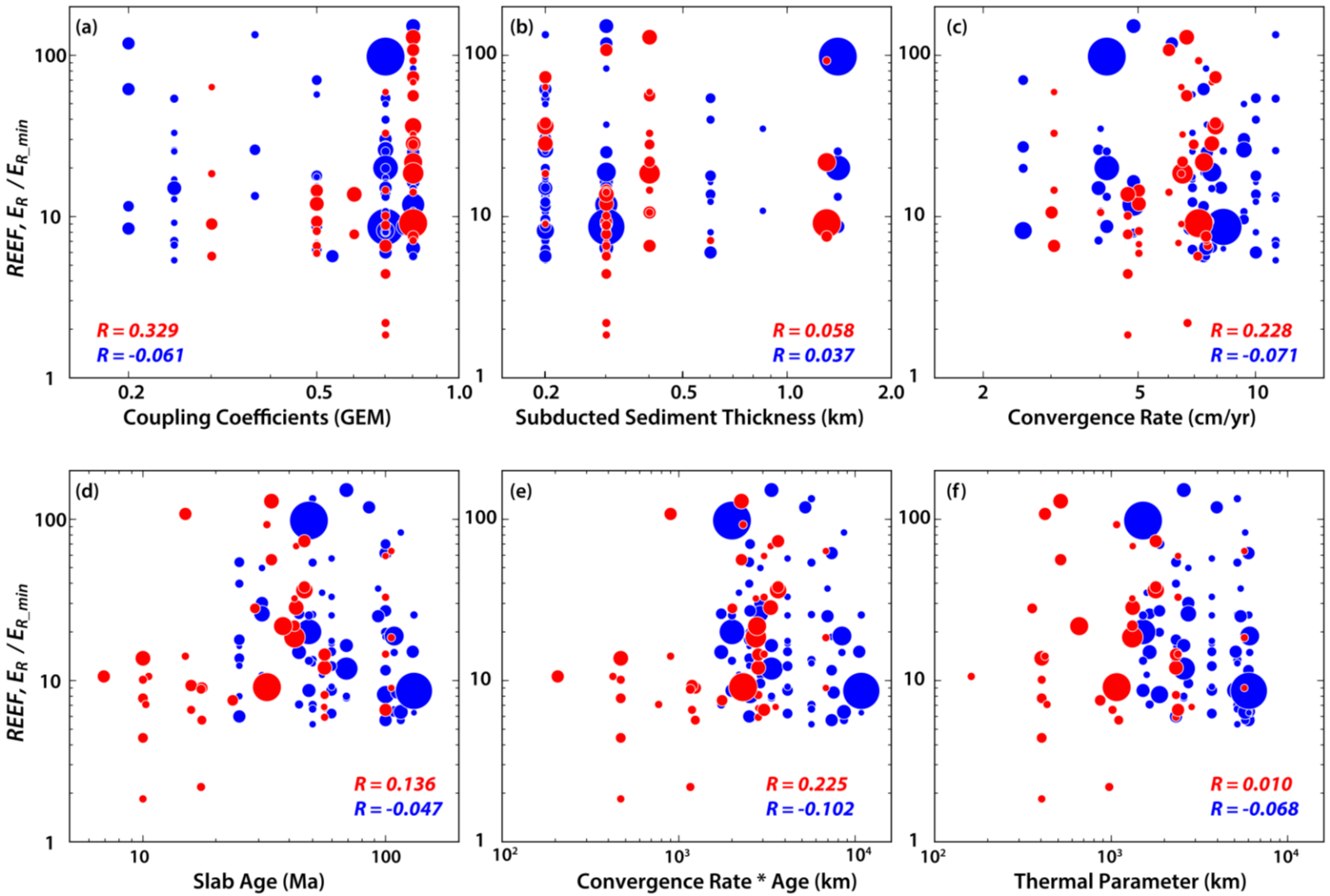


**fig. S10. Comparisons between REEF and subduction zone parameters.** (a) Interseismic coupling coefficients from GEM report[42], (b) subducted sediment thickness from Syracuse et al.[43], (c) convergence rate[43], (d) slab age[43], (e) the product of convergence rate and slab age[43], and (f) thermal parameter[43]. Red and blue dots are for events in Eastern Pacific subduction zones and other regions, respectively. R values in red and blue are their linear correlation coefficients and $R^2$ would give coefficient of determination. Symbol sizes scale with earthquake magnitude.

ScienceAdvances

# Global variations of large megathrust earthquake rupture characteristics

Lingling Ye, Hiroo Kanamori and Thorne Lay

*Sci Adv* **4** (3), eaao4915.
DOI: 10.1126/sciadv.aao4915